



VIBRATION CHARACTERISTICS OF ROCKFILL DAM BASED ON EARTHQUAKE OBSERVATION RECORDS

H. Mogi⁽¹⁾, H. Kawakami⁽²⁾

⁽¹⁾ Associate Professor, Saitama University, hmogi-2008f@kiban.civil.saitama-u.ac.jp

⁽²⁾ Emeritus Professor, Saitama University

Abstract

The Normalized Input-Output Minimization (NIOM) method is applied to long-term seismic records at Aratozawa Dam and the velocity of seismic waves in the embankment is examined. The estimated wave velocity is then used to investigate the vibration characteristics of the embankment. The results revealed that 1) the respective S wave and P wave propagation velocities before the 2008 Iwate-Miyagi Nairiku earthquake were 455 m/s and 1,160 m/s in the upper part of the embankment 626 m/s and 1,479 m/s in the lower part of the embankment; 2) The strong ground motion of the earthquake reduced the S-wave velocity in the upper part of the embankment to about 150 m/s; 3) Analysis of subsequent smaller earthquake records revealed the smaller propagation time more or less in proportion to the logarithm of the number of days passing, and the initial value was restored three years later; 4) A similar change was observed in the 2011 off the Pacific coast of Tohoku earthquake, but the reduction in propagation velocity after the primary motion was less than for the Iwate-Miyagi Nairiku earthquake; and 5) An FE/BE analysis using the estimated propagation velocities yielded a natural frequency for the embankment that is lower than the observed value, so it is necessary to increase the propagation speed in the rock zone to approximate the actual vibration characteristic.

Keywords: rockfill dam, propagation velocity of seismic waves, vibration characteristics, NIOM analysis



1. Introduction

Because soil has a low distortion level that produces nonlinearity and rigidity changes over time due to cementation and changes in pore water pressure, it is difficult to estimate the behavior of soil structures during earthquakes accurately on the basis of laboratory experiments and theoretical analysis alone. Thus, for earth dams and fill dams that have soil as the main material, it is desirable to use actual seismic observation records in addition to experimental data and theoretical values to determine rigidity and strength. For example, Ohmachi *et al.* investigated the velocities of seismic wave propagation in the embankment of the Aratozawa dam based on for the 2008 Iwate-Miyagi Nairiku earthquake and the seismic observation records before and after the earthquake and revealed that 1) the core zone S wave velocity decreased from 500 m/s before the principal motion to 200 m/s in the stream direction and 300 m/s in the dam-axis direction during the principal motion and 2) it took more than one year for the S-wave velocity to recover.

NIOM analysis has been proposed by Kawakami *et al.* as a means for accurate determination of seismic wave propagation time between seismometers and its effectiveness was demonstrated using various observation records.^{2),3)} The NIOM method was applied to data from the Port Island vertical array acquired during the 1995 Hyogoken-Nanbu earthquake, and the results indicated that the correlation between the seismic waves above and below the liquefaction layer was significantly reduced when liquefaction occurred and analysis of aftershocks, including the coda waves of the mainshock, detected a decrease in S-wave velocity.⁴⁾

In the study reported here, the NIOM method was applied to seismic observation records for the Aratozawa Dam (Kurihara City, Miyagi Prefecture, Japan) up to June 2019 and long-term changes in S- and P-wave velocities in the embankment were investigated. The obtained velocity data was then used to investigate the vibration characteristics of the embankment.

2. NIOM method

This section outlines the NIOM method that was developed by Kawakami and Haddadi (1998).

The input-output system can be related by means of a transfer function $H(\omega)$. In the frequency domain, the output $G(\omega)$ is given by

$$G(\omega) = H(\omega)F(\omega), \quad (1)$$

where $F(\omega)$ and $G(\omega)$ are the Fourier transforms of the input $f(t)$ and the output $g(t)$.

Since the transfer function solely depends upon the physical characteristics of the system, we can assume that the same transfer function satisfies the relationship between input and output models. So we can write

$$Y(\omega) = H(\omega)X(\omega), \quad (2)$$

where $X(\omega)$ and $Y(\omega)$ are the Fourier transforms of the input and output models $x(t)$ and $y(t)$, respectively.

The inverse Fourier transform of input model $X(\omega)$ can be written as

$$x(m\Delta t) = \frac{1}{N\Delta t} \sum_{i=0}^{N-1} X(\omega_i) \exp\left(j\frac{2\pi im}{N}\right). \quad (3)$$

At $t = 0$, i.e., $m = 0$, the amplitude of the input model, $x(0)$, is normalized to unity; then equation (3) becomes

$$\frac{1}{N\Delta t} \sum_{i=0}^{N-1} X(\omega_i) = 1. \quad (4)$$

To get the simplified input and output models, the sum of the squared Fourier amplitude and its time



derivatives are minimized subject to the above constraint. Thus, the Lagrange multiplier method gives

$$L = \sum_{i=0}^{N-1} \left[c_X |X(\omega_i)|^2 + k_X \omega_i^2 |X(\omega_i)|^2 + c_Y |Y(\omega_i)|^2 + k_Y \omega_i^2 |Y(\omega_i)|^2 \right] - \lambda \left\{ \frac{1}{N \Delta t} \sum_{i=0}^{N-1} X(\omega_i) - 1 \right\}, \quad (5)$$

where λ is the Lagrange multiplier, c_X and c_Y are the weighing constants for the corresponding squared Fourier amplitude, and k_X and k_Y are the weighing constants for its time derivatives. The same relationship of weighing constants for input and output is considered as

$$\frac{k_X}{c_X} = \frac{k_Y}{c_Y}. \quad (6)$$

The contribution of the high-frequency components can be decreased by increasing the value of k_X .

Substituting equations (2) and (6) into equation (5) and minimizing the equation yields

$$\frac{\partial L}{\partial \lambda} = \frac{\partial L}{\partial X(\omega_i)} = \frac{\partial L}{\partial X^*(\omega_i)} = 0, \quad (i = 0, \dots, N-1), \quad (7)$$

where * denotes the complex conjugate.

After minimization, the input model $X(\omega_i)$ and output model $Y(\omega_i)$ are obtained as follows:

$$X(\omega_i) = N \Delta t \frac{1}{\sum_{n=0}^{N-1} \frac{1}{\left(1 + \frac{k_X}{c_X} \omega_n^2\right) (c_X + c_Y |H(\omega_n)|^2)}}, \quad Y(\omega_i) = H(\omega_i) X(\omega_i). \quad (8)$$

Lastly, the inverse Fourier transforms of the input model $X(\omega)$ and output model $Y(\omega)$ give a simplified input model $x(t)$ and $y(t)$ in the time domain. For the calculation of the inverse Fourier transform using FFT, the first half of the Fourier components of the models were calculated using equation (8), and the number of Fourier components was increased by a factor of 16 by padding trailing zeros in order to interpolate time intervals by 1/16. The latter half of the Fourier components were then set to the complex conjugates of the first half to get real-valued waveforms by using the FFT.

As mentioned above, the NIOM method is a simple input-output analysis technique in which the transfer function is calculated from two observation data satisfying the constraint. It is similar to a receiver function.⁷⁾ In a receiver function, the input $x(t)$ should be a suitable pulse; however, in the NIOM method, adjustment features are included in order to get simplified input and output waveforms.

3. Seismometer arrangement and analysis records for the Aratozawa Dam

We analyzed the acceleration records for three locations in the embankment of the Aratozawa Dam as shown in Fig. 1: inspection gallery L1 (elevation 204 m), the middle of the embankment M1 (elevation 250 m), and the crest T1 (elevation 279 m). The analysis made it possible to estimate the average propagation velocity for the section between L1 and M1 and the section between M1 and T1. Here, we refer to those two sections as the lower section and the upper section. The lower section is 46 m long and the upper section is 29 m long.

The analyzed records include the 2008 Iwate-Miyagi Nairiku earthquake (June 14, 8:43, magnitude 7.2), the 2011 off the Pacific coast of Tohoku earthquake (March 11, 14:46, magnitude 9.0), 302 earthquakes that occurred between July 25, 1992 and October 2, 2001, 683 earthquakes that occurred between the 2008 Iwate-

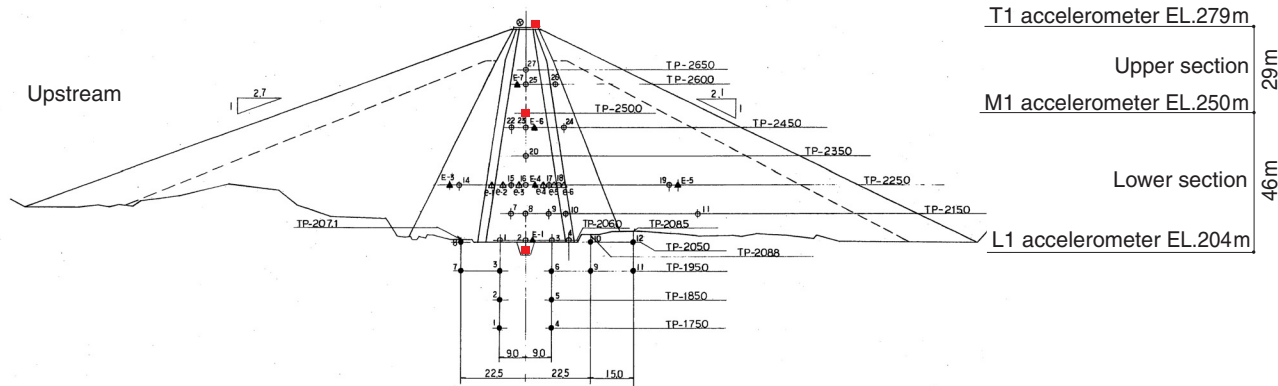


Fig. 1 Cross-section of the Aratozawa Dam, showing seismometer placement.^{5),6)}

Miyagi Nairiku earthquake and the 2011 off the Pacific coast of Tohoku earthquake and 965 earthquakes that occurred between the 2011 off the Pacific coast of Tohoku earthquake and 22:23 on June 18, 2019, for a total of 1,952 earthquakes.

4. Seismic wave propagation velocity in the embankment

4.1 Results of NIOM analysis (input/output model)

Examples of NIOM analysis results for the upper section are presented in Fig. 2 (a) 5.8-magnitude earthquake at 08:10 on 8/11/1996, (b) principal motion of the 2008 Iwate-Miyagi Nairiku earthquake (15 to 21 s), (c) coda waves of the Iwate-Miyagi Nairiku earthquake (450 to 456 s), (d) 3.3-magnitude earthquake at 09:15 on 06/14/2008, (e) 6.8-magnitude earthquake at 00:26 on 7/24/2008 on the Iwate coast, (f) principal motion of the 2011 off the Pacific coast of Tohoku earthquake (39 to 43 s), (g) coda waves of the off the Pacific coast of Tohoku earthquake (585 to 589 s), and (h) 7.2-magnitude earthquake at 23:33 on 4/7/2011 off Miyagi prefecture. In Fig. 2, the solid red line, solid blue line, and solid black line respectively represent the output model (simplified waveform of the lower seismometer) for the stream component, the dam-axis component, and the vertical component. Although the input model is shown only for the stream component in the figure, the waveforms from the upper and lower seismometers for the same direction are used in the calculations for the analysis.

Taking the time in which a pulse of unit amplitude passes through the upper seismometer (T1, stream component) as time 0 (thin broken black line in Fig. 2), we see that the same pulse passes through the lower seismometer (M1) at -0.07250 s (peak of the red line). The propagation time of the S wave oscillating in the stream direction was therefore 0.0725 seconds in this earthquake. Similarly, we see that the propagation time of the S wave oscillating in the dam axis direction during the earthquake was 0.07187 s (solid blue line in the figure). The propagation time for the vertical component, on the other hand, was 0.0275 seconds (black solid line in the figure), indicating a shorter propagation time than for the two horizontal components. Seismic waves generally undergo repeated refraction as they propagate from the hypocenter, and so impinge in a nearly vertical direction near the surface. For that reason, the waves oscillating in the vertical direction are mainly P waves and propagation time estimated from the vertical component represents the propagation time of the P wave.

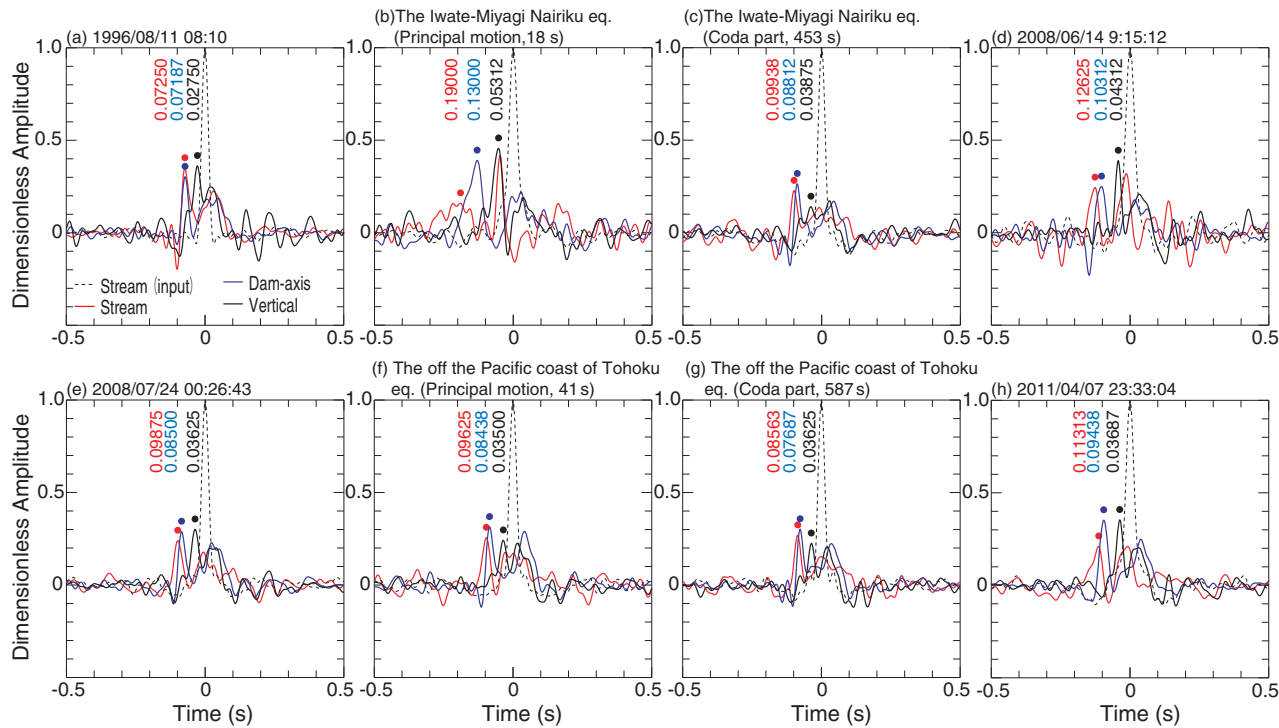


Fig. 2 Example of NIOM analysis for the upper section (accelerometer T1 and M1). The output models (simplified waveform of the lower accelerometer, M1) are shown by the solid lines (red: stream component; blue: dam-axis component; black: vertical component) the broken black line represents the input model for the stream component (simplified waveform of the upper accelerometer, T1).

4.2 Temporal change in propagation time

The propagation times for all the seismic records processed by the method described in section 4.1 are presented in Fig. 3 for the upper section and Fig. 4 for the lower section. In both figures, the results for the 302 earthquakes between July 1992 and October 2001 are presented in (a), the results for the changes during the principal motion of the Iwate-Miyagi Nairiku earthquake are presented in (b), the results for the minor earthquakes that occurred between immediately after the Iwate-Miyagi Nairiku earthquake and before the 2011 off the Pacific coast of Tohoku earthquake are presented in (c), the temporal changes during the principal motion of the 2011 off the Pacific coast of Tohoku earthquake are presented in (d), and results of subsequent minor earthquakes are presented in (e). In the figures, red points represent the results for the stream component, blue points represent the results for the dam-axis component, and black points represent the results for the vertical component. The root mean square of the velocity amplitude in each time window for which the NIOM analysis was performed is shown below each figure as an index of ground motion intensity.

The horizontal broken lines in Figs. 3 and 4 indicate the average propagation time for the 302 earthquakes that occurred between 1992 and 2001. The values are 0.0637 s for the upper section (equivalent to a propagation velocity of 455.3 m/s), 0.0667 s (434.8 m/s) for the dam-axis component, and 0.0250 s (1,160.0 m/s) for the vertical component. The respective values for the lower section are 0.0735 s (625.9 m/s), 0.0753 s (610.9 m/s), and 0.0311 s (1,479.1 m/s). We use these values for comparison with the results for after the Iwate-Miyagi Nairiku earthquake.

The results presented in Fig. 3 (b) show that very strong ground motion (velocity amplitude RMS values of 33.6 cm/s (stream component) and 23.8 cm/s (dam-axis component)) was produced

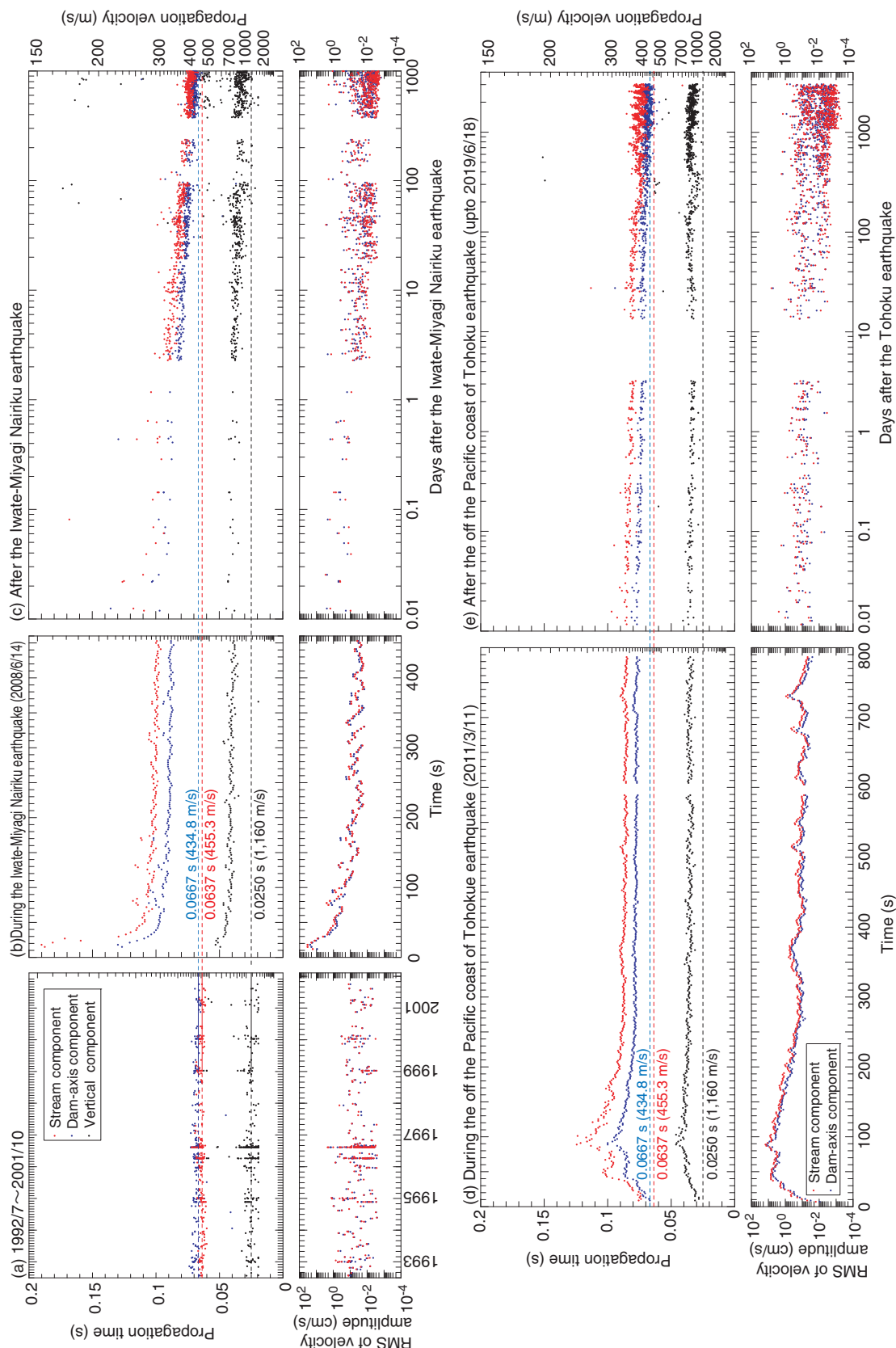


Fig. 3 NIOM analysis results for the 2008 Iwate-Miyagi Nairiku earthquake and the 2011 off the Pacific coast of Tohoku earthquake, including the propagation times before and after the earthquakes in the upper section.

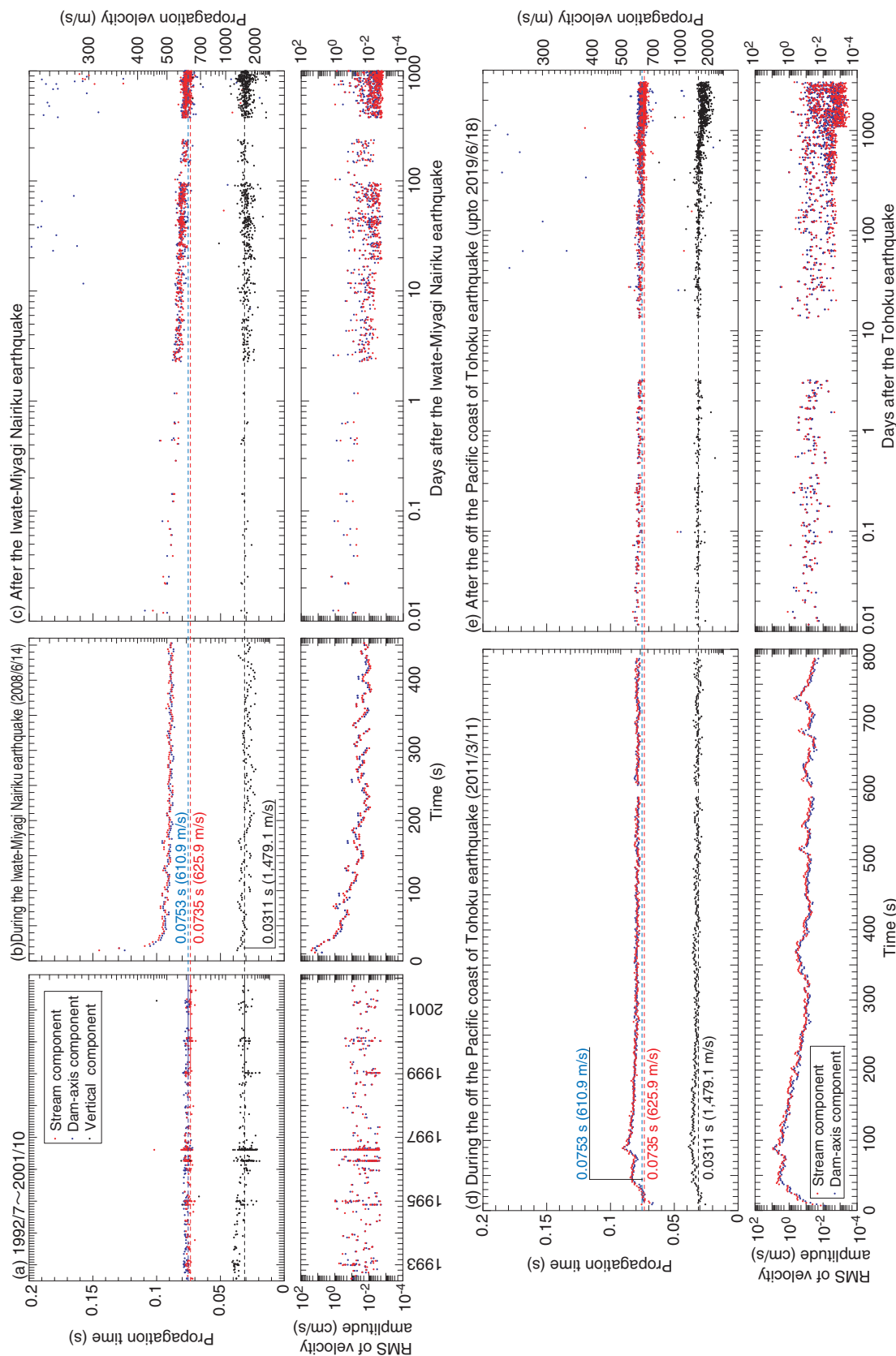


Fig. 4 NIOM analysis results for the 2008 Iwate-Miyagi Nairiku earthquake and the 2011 off the Pacific coast of Tohoku earthquake, including the propagation times before and after the earthquakes in the lower section.

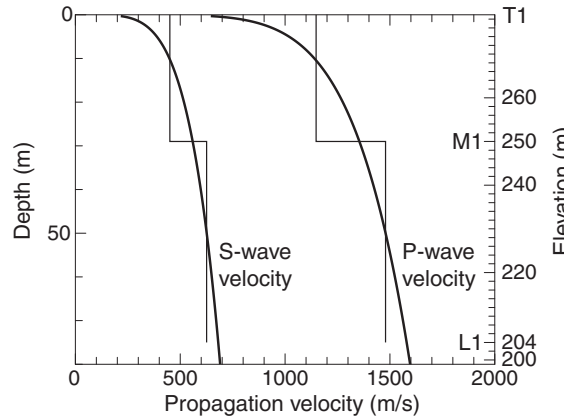


Fig. 5 Comparison of the mean section propagation times obtained by NIOM analysis and the velocity distribution equations

in the principal motion of the Iwate-Miyagi Nairiku earthquake. The propagation velocities increased to 0.190 seconds (propagation velocity of 153 m/s) for the stream component and to 0.130 seconds (223 m/s) for the dam-axis component. The propagation time decreases sharply with the decrease in ground motion amplitude, but does not return to the value prior to the earthquake estimated from the analysis of earthquakes before 2001, even after 400 seconds. Analysis results for the subsequent minor earthquakes (Fig. 3c) show that the propagation time decreases in proportion to the logarithm of the number of elapsed days. Return to the original value thus required about three years.

Similar changes are exhibited in the analysis results for the principal motion of the 2011 off the Pacific coast of Tohoku earthquake (Fig. 3d) and subsequent minor earthquakes (Fig. 3e), but the RMS values for the velocity amplitude for the 2011 off the Pacific coast of Tohoku earthquake (7.2 cm/s for the stream component and 5.8 cm/s for the dam-axis component) are lower than for the Iwate-Miyagi earthquake and the increase in propagation time is no more than 0.104 s (propagation velocity of 279 m/s) for the stream component and no more than 0.088 s (330 m/s) for the dam-axis component. The long duration of ground movement in the 2011 off the Pacific coast of Tohoku earthquake is a concern, but the 2011 off the Pacific coast of Tohoku earthquake is considered to have had no major effect on the embankment of the Aratozawa dam.

For the earthquakes up to 2001, there was no significant difference in the S-wave velocities of the stream component and the dam-axis component, but the differences in propagation velocities are seen after the Iwate-Miyagi Nairiku earthquake. We can therefore conclude that significantly strong ground motion may result in polarization anisotropy. A similar change is seen in the propagation time of the vertical component, and the P-wave velocity exhibits the same nonlinear behavior as the S wave. The propagation time in the lower section (Fig. 4) also exhibits the similar nonlinear behavior seen in the upper section, but the propagation velocities for the stream component and the dam-axis component are about the same and there is no polarization anisotropy between the two horizontal components.

4.3 Distribution of S-wave velocities

Considering that the shear modulus of soil materials is generally strongly governed by the confining pressure,⁸⁾ we assumed the following relationship.

$$G \propto z^\beta \quad (9)$$

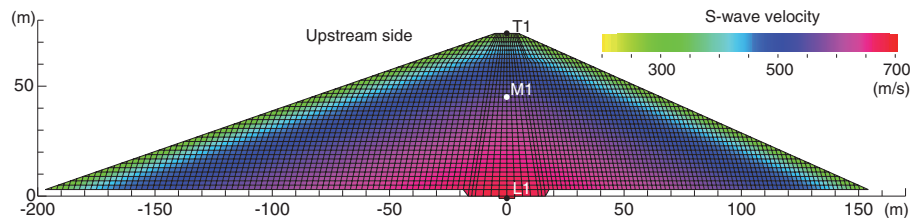


Fig. 6 FEM model and S-wave velocity distribution (Case 1)

Where G represents the shear modulus, z is the depth from the crest and β is an unknown constant. From $G = \rho V^2$ (where ρ is density), the S-wave velocity V can be expressed as the following equation using unknown constants α and β .

$$V(z) = \alpha z^{\beta/2} \quad (10)$$

Applying Eq. (10), the S-wave propagation time from depths Z_2 to Z_1 (where $Z_2 > Z_1$) is expressed by the following equation.

$$t = \int_{Z_1}^{Z_2} \frac{dz}{V(z)} = \frac{2}{\alpha(2-\beta)} \left\{ Z_2^{(2-\beta)/2} - Z_1^{(2-\beta)/2} \right\} \quad (11)$$

We use the propagation times obtained in this study for the stream components (upper section: 0.6370 s; lower section: 0.0735 s) and vertical components (upper section: 0.0250 s; lower section 0.0311 s) up to October 2001. We used Eq. (11) to obtain the S- and P-wave velocity distributions. The obtained distributions are shown in Fig. 5 and Eqs. (12) and (13).

$$V_S(z) = 278.1 z^{0.415/2} \text{ m/s} \quad (12)$$

$$V_P(z) = 784.9 z^{0.324/2} \text{ m/s} \quad (13)$$

5. Two-dimensional FE/BE method analysis

5.1 Analytical model

The finite element method (FEM) model for the embankment (Fig. 6) has 3,455 nodes (6910 degrees of freedom) and 3,328 elements. Four-node iso-parametric elements and linear triangular elements were used in the modeling. Based on the PS logging results,⁹⁾ we assumed that the foundation is a uniform semi-infinite body that has a P-wave velocity of 3,500 m/s, an S-wave velocity of 1800 m/s (Poisson ratio of 0.32), and a density of 2,400 kg/m³. The upstream and downstream sides of the embankment were both modeled by the boundary element method (BEM) over the range of 600 m from the toe of the embankment. The model uses 300 elements, with linear elements for displacement and constant elements for surface force. The nodes at the interface of the embankment and foundation are shared with the FEM nodes of the interface, and seismic motion was input by applying a planar SV wave to the BEM model.

Two cases are set for the velocities of the S wave and P wave in the embankment. Case 1 is the model with the propagation velocities given by Eqs. (12) and (13) obtained from the vertical distance from the center point of each finite element to the surface of the embankment directly above it. Case 2 is 1.2 times the propagation velocity in the rock zone and the filter zone in Case 1. The S-wave velocity distribution for Case 1 is shown in Fig. 6. Taking the density of the embankment to be the

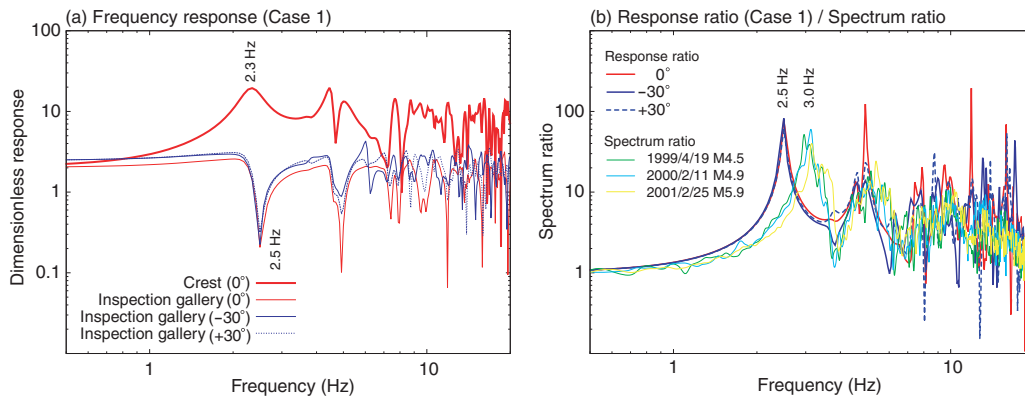


Fig. 7 Analysis results for Case 1: (a) Frequency response function for the crest and the inspection gallery obtained by FE/BE analysis, (b) Comparison of the ratio of response functions for the crest and inspection gallery and the observed spectrum ratios.

same for both cases, the values are $1,970 \text{ kg/m}^3$ for the core zone, $2,210 \text{ kg/m}^3$ for the upstream rock zone, and $2,120 \text{ kg/m}^3$ for the downstream rock zone.⁵⁾ We assume that there is no damping in the embankment because the amplitudes of the earthquakes used in the comparison are small. In the analysis, we obtained the frequency response to the vertical SV wave incidence for 512 frequency components up to 40 Hz and then obtained the time history response to the Gaussian pulse by FFT after padding the trailing zeros up to 160 Hz.

5.2 Analysis results

For Case 1, the frequency response function is shown in Fig. 7(a) and the response function ratio between the crest and inspection gallery as well as the spectrum ratios for the seismic records in the crest and inspection gallery are presented in Fig. 7(b). In the frequency response function at the inspection gallery (Fig. 7a), we see a steep valley near 2.5 Hz, which is the fundamental frequency of the embankment. The peak response at the crest of the embankment, on the other hand, appears at 2.3 Hz, slightly lower than the natural frequency. Although steep valleys also occur at frequencies above 5 Hz at the inspection gallery, the frequencies at which the valleys occur vary with the angle of incidence in the results for oblique angles of incidence on the upstream side ($+30^\circ$) and the downstream side (-30°). We consider the reason that clear peak and valley shapes do not appear for higher frequencies in the crest/inspection gallery spectrum ratios for actual seismic records (Fig. 8a) to be superimposition of seismic waves propagating in various directions.

The propagation times calculated from the time history response for Case 1 is 0.0684 s between L1 and M1 and 0.0734 s between T1 and M1, which are close to observed ones. The response function ratio for the crest and the inspection gallery has a peak at 2.5 Hz, but the spectral ratio between the crest and the inspection gallery obtained from the seismic records has a peak near 3.0 Hz, and the fundamental frequency is inconsistent with the observation results.

The frequency response function and pulse response waveform for Case 2 are presented in Fig. 8, where we can see that increasing the rigidity of the rock zone increases the fundamental frequency, making the obtained results consistent with the spectrum ratio of the observed waveforms. On the other hand, the propagation time in the core zone is slightly less than the observed propagation time. From those results, we can understand that while the fundamental frequency is mainly affected by the physical properties in the rock zone that has a large cross-section, the propagation velocity of seismic waves obtained by NIOM analysis reflects the physical properties in the core zone.

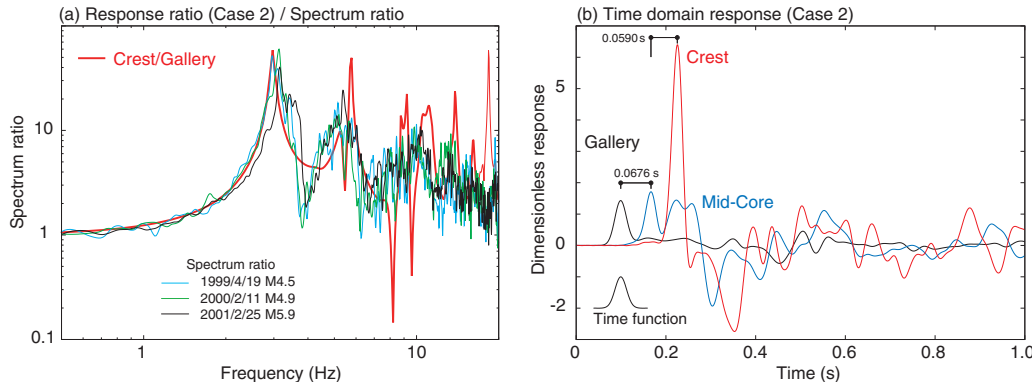


Fig. 8 Analysis results for Case 2: (a) Comparison of the ratio of response functions for the crest and inspection gallery obtained by FE/BE analysis and the observed spectrum ratios, (b) Response waveforms for the crest, the middle of the core zone, and the inspection gallery due to the vertical incidence of a Gaussian pulse.

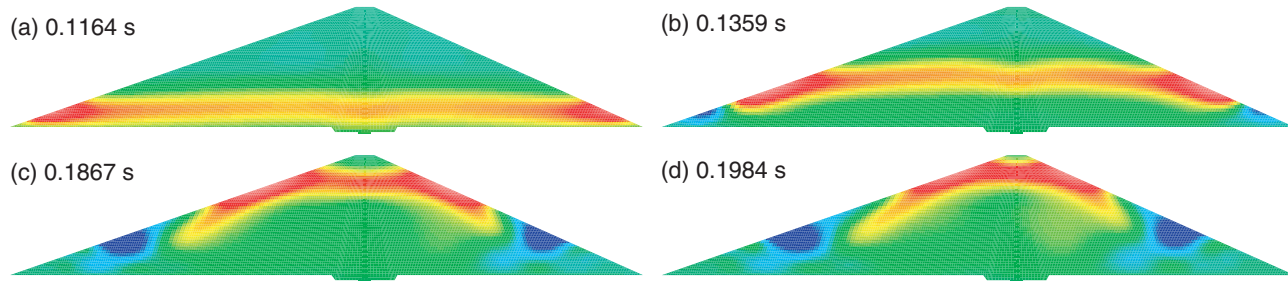


Fig. 9 Snapshots of the pulse response for Case 2.

From snapshots of the pulse wave propagation (Fig. 9), we can see that the wavefront in the rock zone where the confining pressure is high advances first near the center of the embankment. The wavefront in the embankment thus becomes curved and propagates. As the wavefront approaches the crest, the wave motion that is propagating upward in the core zone and the wave motion that is propagating around the rock zone are superimposed. Thus, the propagation time estimated by NIOM analysis is affected by the superimposition of waves from the rock zone and waves from the core zone. This suggests that accurate evaluation of the properties of wave propagation in the embankment is required for accurate determination of the physical properties of the embankment from the seismic records.

6. Conclusion

We investigated the propagation time (velocity) of seismic waves in the embankment of the Aratozawa Dam in Kurihara City, Miyagi Prefecture, Japan by NIOM analysis of long-term observation accelerograms. We also investigated the vibration characteristics of the embankment based on the obtained propagation velocities. The main results are listed below.

1. The seismic wave propagation times before the 2008 Iwate-Miyagi Nairiku earthquake were 0.0637 s (corresponding velocity of 455.3 m/s) for the stream component, 0.0667 s (434.8 m/s) for the dam-axis component, and 0.0250 s (1,160.0 m/s) for the vertical component in the upper section. In the lower section, the respective times were 0.0735 s (625.9 m/s), 0.0753 s (610.9 m/s), and 0.0311 s



(1,479.1 m/s).

2. The strong ground motion of the Iwate-Miyagi Nairiku earthquake increased the propagation times for the stream component to about 0.190 seconds (153 m/s) and to about 0.130 seconds (223 m/s) for the dam-axis component. Subsequently, the propagation times decrease rapidly as the amplitude of the seismic motion decreases, but the values do not return to the values prior to 2001 Earthquake, even after 400 s.
3. In subsequent minor earthquakes, propagation times decrease in proportion to the logarithm of the number of elapsed days, and about three years are required for the original values to return.
4. Although a similar change was observed in the 2011 off the Pacific coast of Tohoku earthquake the increase in propagation times after the principal motion was smaller than seen in the Iwate-Miyagi Nairiku earthquake, and the effect was judged to be insignificant.
5. We estimated the distribution of propagation velocity in the embankment on the basis of propagation times obtained by NIOM analysis. In the results of the FE/BE analysis, the propagation time values are close, but the value for the fundamental frequency of the embankment is lower than the observed value. However, a model in which the propagation velocity in the rock zone and the filter zone is increased by 20% can explain the fundamental frequency. That indicates that the vibration characteristic of the embankment is strongly influenced by the rock zone.

Acknowledgement

In the work described here, we analyzed valuable observation records for Aratozawa Dam that were provided by Kurihara District Dam General Office of Miyagi Prefecture and used the results to offer a detailed explanation of the dam embankment and observation records. We wish to thank the staffs of the Kurihara District Dam General Office, and all other involved persons for cooperation in this work. This research was supported by JSPS Grants-In-Aid for Scientific Research, Fundamental Research (C) 17K06528, "Investigation of Seismic Wave Propagation Velocity in a Filldam". We extend special gratitude to all concerned.

References

- [1] Ohmachi, T., Tahara, T. (2011): Nonlinear earthquake response characteristics of a central clay core rockfill dam, *Soils and Foundations*, **51**(2), 227–238.
- [2] Kawakami, H., Haddadi, H. R. (1998): Modeling wave propagation by using Normalized Input-Output Minimization (NIOM), *Soil Dyn. Earthq. Engng.*, **17**, 117–126.
- [3] Haddadi, H. R., Kawakami, H. (1998): Modeling wave propagation by using Normalized Input-Output Minimization (NIOM) method for multiple linear systems, *Structural Eng./Earthquake Eng.*, *JSCE*, **15**, 29s–39s.
- [4] Hadaddi, H. R., Kawakami, H. (1998): Effect of liquefaction on ground motion during the Hyogoken-nanbu earthquake, 1995, in Japan by using NIOM method, The Effect of Surface Geology on Seismic Motion, Irikura, Kudo, Okada and Sasatani (eds), Balkema, Rotterdam, **2**, 1015–1022.
- [5] Tohoku Regional Agricultural Administration Office, Ministry of Agriculture, Forestry and Fisheries (1993): Technical Report of Aratozawa Dam, (*in Japanese*).
- [6] Kurihara District Dam General Office (2008): March 2008 report on embankment inspection of Aratozawa Dam, (*in Japanese*).
- [7] Langston, C. A. (1979): Structure under Mount Rainier, Washington, inferred from teleseismic body waves, *J. Geophys. Res.*, **84**, 4749–4762.
- [8] Ishihara, K. (1996): Soil Behaviour in Earthquake Geotechnics, Oxford Science Publications.
- [9] Japan Commission on Large Dams (2018): Report of WG for Estimation of Input Earthquake Motions and Earthquake Resistance of Dams, Large Dams, **243**, 4–46, (*in Japanese*).